Finite-Cloud Effects in Longwave Radiative Transfer

ANDREW K. HEIDINGER AND STEPHEN K. COX

Department of Atmospheric Science, Colorado State University, Fort Collins, Colorado

(Manuscript received 13 March 1995, in final form 28 September 1995)

ABSTRACT

As numerical weather and climate prediction models demand more accurate treatment of clouds, the role of finite-cloud effects in longwave radiative transfer clearly warrants further study. In this research, finite-cloud effects are defined as the influence of cloud shape, size, and spatial arrangement on longwave radiative transfer. To show the magnitude of these effects, radiometer data collected in 1992 during the Atlantic Stratocumulus Transition Experiment (ASTEX) were analyzed. The ASTEX data showed that radiative transfer calculations that ignored the vertical dimensions of the clouds underestimated the longwave cloud radiative surface forcing by 30%, on average. To study further these finite-cloud effects, a three-dimensional 11-μm radiative transfer model was developed. Results from this model, which neglected scattering, agreed with the measurements taken during ASTEX on 14 June 1992. This model was also used to reiterate that, for optically thick clouds, knowledge of cloud macrophysical properties can be more crucial to the modeling of the transfer of longwave radiation than the detailed description of cloud microphysical properties. Lastly, techniques for the inclusion of these finite-cloud effects in numerical models were explored. Accurate radiative heating rate profiles were achieved with a method that assumed a linear variation of the cloud fraction within the cloud layer. Parameterizations of the finite-cloud effects for the marine stratocumulus observed during ASTEX are presented.

1. Introduction

Clouds have long been known to be the most variable component of the earth's climate system. The recent advances in satellite remote sensing and three-dimensional radiative transfer have clearly demonstrated that the plane-parallel approximation for radiative transfer in the presence of clouds is not valid over significant regions of the globe. For example, the work of Niylisk (1972) over two decades ago used the cumulus observations of Plank (1969) to simulate the errors in the longwave surface flux estimates from modified plane-parallel calculations. His results showed that the average error in the longwave surface radiative forcing was roughly 20% for the cloud fields simulated.

In contrast to plane-parallel clouds, which are infinite in horizontal extent, finite clouds are defined as any clouds with both finite horizontal and vertical dimensions. Accordingly, finite cloud effects can be defined as the difference between any longwave radiative quantity measured or computed in the presence of three-dimensional finite clouds and that predicted by modified plane-parallel calculations that treat clouds two dimensionally. This study will focus on finite cloud effects in longwave surface fluxes and heating rates. In this study, modified plane parallel will refer to the commonly used method of weighting plane-parallel calculations by the cloud fraction to account for partial cloudiness.

The transfer of longwave radiation through isolated cubic clouds has been studied previously by Liou and Ou (1979), Harshvardhan et al. (1981), and Stephens and Preisendorfer (1984). These results showed that isolated cubic clouds exhibit stronger cooling than plane-parallel clouds due to the enhanced cooling near the lateral boundaries of the cubic clouds.

The transfer of longwave radiation through layers of finite clouds has been addressed by Niylisk (1968, 1972), Ellingson (1982), Harshvardhan and Weinman (1982), Evans (1993), and Killen and Ellingson (1994). The results from these studies were concerned primarily with fluxes exiting layers of finite clouds.

With the results from the previous work in mind, the goals of this work are as follows: 1) To quantify the finite-cloud effects in longwave radiation through the analysis of actual radiometer data. 2) To develop and compare methods for the inclusion of these finite-cloud effects into the one-dimensional radiative transfer schemes used in numerical weather and climate prediction models. The completion of the second goal required the development of a three-dimensional longwave radiative transfer model. Results from this model

Corresponding author address: Andrew K. Heidinger, Department of Atmospheric Science, Colorado State University, Fort Collins, CO 80523.

will also be compared to the measurements used in fulfilling the first goal.

2. The ASTEX observations

Though finite-cloud effects have been studied previously, direct measurements of finite-cloud effects are rare. In this section, results from an analysis of the surface radiometer data from the Atlantic Stratocumulus Experiment (ASTEX) are presented.

The ASTEX phase of the First ISCCP (International Satellite Cloud Climatology Project) Regional Experiment Phase II (FIRE II) took place during June 1992 on and near the island of Porto Santo in the Madeira Islands. The ASTEX Porto Santo datasets are described by Cox et al. (1993). One reason for choosing this region was that it offered an opportunity to study the transition from the marine stratus to the stratocumulus cloud regime. This region was highly suitable for studying finite cloud effects since single broken layers of boundary layer clouds were often observed with cloud fractions ranging from near-clear to overcast conditions. The surface measurement site was located on a 100-m cliff near the northwest corner of the island.

One important quantity in studying cloudiness effects on the surface energy budget is longwave cloud radiative surface forcing, $CF(S)_{lw}$. In this study, values of $CF(S)_{lw}$ are defined as

$$CF(S)_{lw} = F_{sfc} - F_{sfc,clr}, \quad (1)$$

where F_{sfc} is the observed downwelling broadband surface flux and $F_{sfc,clr}$ is the value of F_{sfc} for clear sky conditions. Values of F_{sfc} were measured during ASTEX using a 4–50-μm pyrgeometer, which was calibrated using the method described in Albrecht and Cox (1976). Due to the rare occurrence of clear conditions during ASTEX preventing the direct measurements of $F_{sfc,clr}$, values of $F_{sfc,clr}$ were obtained using LOWTRAN 7, a 20 cm^{-1} spectral resolution radiative transfer model developed by the Air Force Geophysics Laboratory. Using LOWTRAN, values of $F_{sfc,clr}$ ranged from approximately 290 to 360 W m^{-2} during ASTEX, which corresponded to values of the rawinsonde-derived precipitable water values of 1.7 and 4.7 cm, respectively. Comparison of the available clear sky measurements of $F_{sfc,clr}$ with the LOWTRAN values showed that the use of LOWTRAN was accurate to within 5 W m^{-2}.

The observed daily variation of the $CF(S)_{lw}$ during ASTEX is presented in Fig. 1, which shows that the daily averaged values ranged from near 0 to over 50 W m^{-2} with a period mean of 30 W m^{-2}. This average value for $CF(s)_{lw}$ from the surface radiometer measurements from June 1992 on Porto Santo is consistent with the value of 30–40 W m^{-2} for this region for July 1985 published by Gupta et al. (1993) using ISSCP 2.5° resolution data.

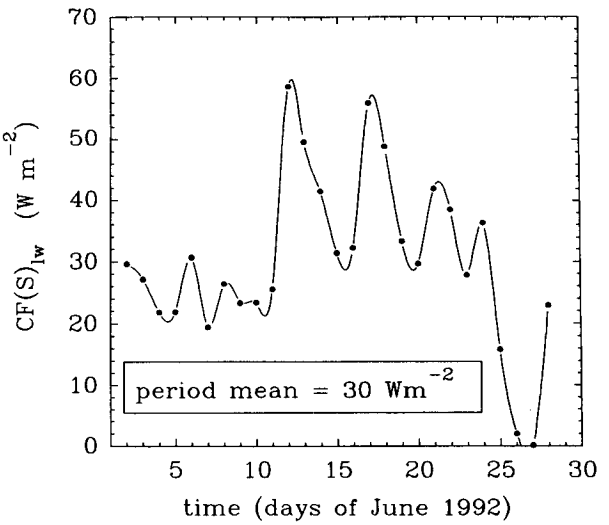

FIG. 1. The observed daily $CF(S)_{lw}$ during ASTEX.

a. Finite-cloud surface flux enhancement

One meaningful way to show finite-cloud effects in longwave radiative transfer is to show the effect of finite clouds on the values of $CF(S)_{lw}$. This effect can be computed as the difference in the $CF(S)_{lw}$ values measured in the presence of three-dimensional finite clouds and that calculated assuming two-dimensional or planar clouds, $CF(S)_{lw,2D}$. Symbolically, we can therefore define a finite-cloud effect flux, F_{fce}, as

$$\begin{aligned} F_{fce} &= CF(S)_{lw} - CF(S)_{lw,2D} \\ &= (N_e - N_a)(F_{sfc,ovc} - F_{sfc,clr}). \end{aligned} \quad (2)$$

The values of $CF(S)_{lw,2D}$ can be computed as

$$CF(S)_{lw,2D} = N_a(F_{sfc,ovc} - F_{sfc,clr}), \quad (3)$$

where N_a is the absolute cloud fraction and F_{ovc} is the downwelling longwave flux at the surface under overcast sky conditions. Here, N_e represents the effective cloud fraction and is discussed in section 2c. Physically, F_{fce} represents the enhancement of the longwave surface forcing due to the emission from the lateral cloud boundaries. The absolute cloud fraction N_a accounts only for the horizontal projection of the clouds while neglecting any contributions of the cloud's vertical dimensions on the cloud cover. Typically, most numerical weather prediction models account for partial cloudiness with cloud fractions that are equivalent to N_a. In this study, values of N_a were computed on an hourly basis using a simple threshold analysis on the data from a PRT-6 radiometer. The PRT-6 used a 2° field of view in this application and viewed the zenith with a spectral bandpass centered on 11 μm. PRT-6 measurements with 11-μm equivalent brightness temperatures (EBT) greater than 260 K were interpreted

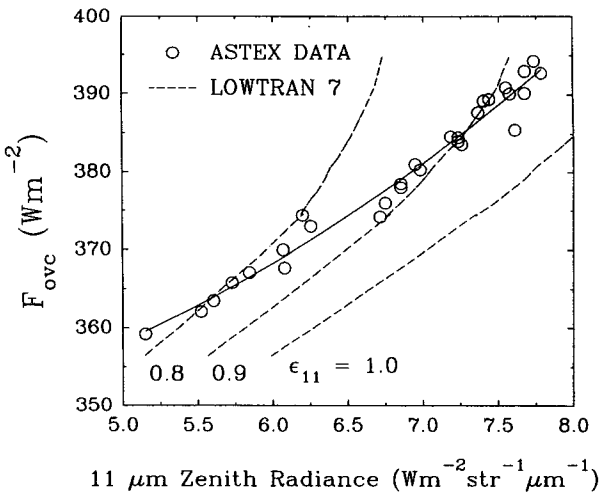

FIG. 2. Measured and modeled variations of the broadband overcast surface flux with the 11-μm zenith radiance. Modeled results generated using LOWTRAN 7 with differing values of the 11-μm cloud emissivity ϵ_{11}.

as measurements of clouds. This threshold EBT value was chosen since it represented the lowest observed EBT during known overcast conditions. Only during periods with low cloud fractions was the cloud fraction measured with the PRT-6 sensitive to the value of the threshold EBT. Accordingly, the cloud-forcing data presented here were little affected by the value of the threshold used.

Before values of F_{fce} defined in Eq. (2) could be calculated, values of F_{ovc} needed to be computed for the entire period. The calculation of F_{ovc} in this study was accomplished through an empirical relation between the 11-μm downwelling zenith radiance measured by the PRT-6, R_{11}, and the downwelling overcast sky flux measured by the pyrgeometer, F_{ovc}, during known periods of overcast sky conditions. The ceilometer-derived cloud bases of these overcast sky measurements ranged from 200 to 1800 m. The observed relation between R_{11} (W m^{-2} μm^{-1} str^{-1}) and F_{ovc} (W m^{-2}) is shown in Fig. 2 as the solid line and can be expressed as

$$F_{ovc} = 1.4R_{11}^2 - 5.4R_{11} + 350.2. \quad (4)$$

Due to the abundance of cloudy PRT-6 measurements, even during periods of sparse cloud cover, values of F_{ovc} could be generated using Eq. (4) for most of the ASTEX period. During the rare occurrences of clear sky conditions, values of F_{ovc} were interpolated from the available data. Since the PRT-6 measurements were confined to a 2° field of view, the lateral flux leakage occurring in clouds caused no significant error in the estimation of F_{ovc} during periods of broken cloudiness.

In addition to the ASTEX measurements shown in Fig. 2, simulations of the variation of the PRT-6 and pyrgeometer readings were generated using LOWTRAN. Each dashed line in Fig. 2 represents a different value of the 11-μm emissivity, ϵ_{11}, of the clouds used in the LOWTRAN simulations. Due to the opacity of liquid water through most of the longwave spectral region, the broadband cloud emissivities were assumed to be 1.0 in these simulations. Any contribution from the atmosphere above the cloud layer was ignored. The LOWTRAN-generated values were obtained by positioning the clouds at different levels in an average ASTEX sounding. The clouds were assumed to radiate at the cloud-base temperature. A comparison of the ASTEX data and the LOWTRAN simulations showed an apparent decrease in ϵ_{11} with decreasing values of F_{ovc} and R_{11}. This can probably be explained by a systematic decrease in the cloud thickness with increasing cloud base for the marine stratocumulus clouds during ASTEX (Heidinger and Cox 1994).

Now that values of F_{ovc} could be generated from the ASTEX data, the finite-cloud effects in the values of $CF(S)_{lw}$ defined in Eq. (2) could be computed. The daily variation during ASTEX of the quantity F_{fce} is shown in Fig. 3. The relative minima in Fig. 3 are associated with clear or near-overcast days where finite-cloud effects would be expected to be minimal. The period mean of the F_{fce} values at ASTEX was approximately 9 W m^{-2}, with the daily values ranging from near 0 to over 15 W m^{-2}. This period-mean value of F_{fce} is roughly twice the value derived from the results of Niylisk (1972). The magnitude of these effects is roughly 30% of the observed-mean $CF(S)_{lw}$. Therefore, any scheme that calculated $CF(S)_{lw}$ and ignored the contribution of the emission from cloud sides would tend to underestimate the true value by approximately

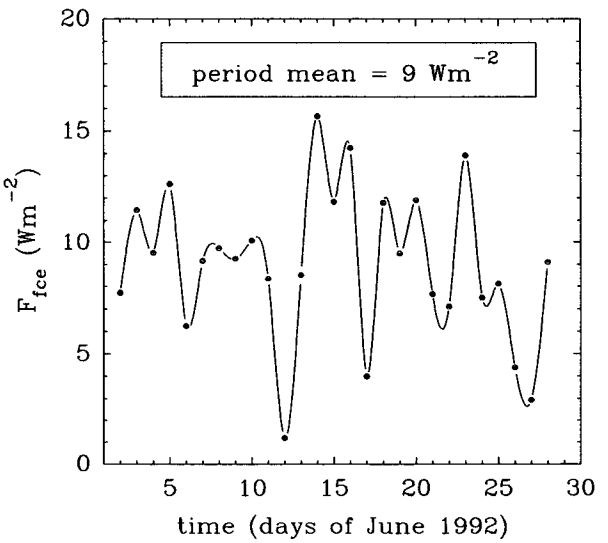

FIG. 3. Observed daily variation in the finite-cloud effect flux F_{fce} during ASTEX.

50% during the ASTEX period. Clearly, any surface energy budget study in the presence of partial cloudiness with a desired accuracy of 20 W m^{-2} or less needs to account for these effects.

As stated above, the period mean value of F_{fce} during ASTEX was 9 W m^{-2}. Knowing that the observed values of $F_{sfc,ovc} - F_{sfc,clr}$ during ASTEX ranged from approximately 40 to 80 W m^{-2}, one can see from Eq. (2) that errors of 0.1 in the observed values of N_a could result in errors in F_{fce} that are nearly as large as the observed-period mean. Though no reason exists to believe that the measured values of N_a were systematically in error, these potential errors need to be kept in mind when interpreting the values of F_{fce} presented here.

b. *Observed finite-cloud effects on 14 June 1992*

An illustrative example of the role of finite-cloud effects on the $CF(S)_{lw}$ can be seen by analyzing the variation of $CF(S)_{lw}$ on 14 June 1992 during ASTEX. Though the measured cloud fraction N_a decreased from approximately 1.0 to 0.4 at 0600 and 1200 UTC, the observed $CF(S)_{lw}$, shown in Fig. 4, did not show a corresponding large decrease. One possible reason for the observed variation of the $CF(S)_{lw}$ during this 0600–1200 UTC period is the buffering effect of lateral cloud side emission keeping the $CF(S)_{lw}$ relatively large. Also shown in Fig. 4 is the variation of $CF(S)_{lw,2D}$ on 14 June. Analysis of Fig. 4 shows that the values F_{fce} greater than 30 W m^{-2} were observed during the 0600–1200 UTC period, with smaller values of F_{fce} being seen in the near overcast period before 0600 UTC and the near-clear period after 1500 UTC.

Also shown in Fig. 4 are model simulations of the variation of the $CF(S)_{lw}$ on 14 June. The model is described in the next section. Broadband values were computed from the 11-μm radiative transfer model by assuming the clouds were graybodies and forming an empirical relation between the broadband and 11-μm surface radiance using LOWTRAN. The cloud layer on 14 June was simulated as a layer of cuboidal clouds distributed regularly on a horizontal plane. The term *cuboidal clouds* refers to rectangular clouds with equal horizontal dimensions. Rough estimates of the cloud horizontal dimensions were made by using the PRT-6 to compute the length of time for clouds to pass overhead and assuming that the clouds moved at the mean wind speed through the cloud layer, which was observed by rawinsondes to be approximately 12 m s^{-1} on this day. The vertical dimension of the cloud layer, which varied from 100 to 500 m, was derived from measurements taken by the National Oceanic and Atmospheric Administration/Environmental Research Laboratory (NOAA/ERL) 8.7-mm radar. Using these hourly-averaged horizontal and vertical dimensions along with the measured values of N_a, the cloud field

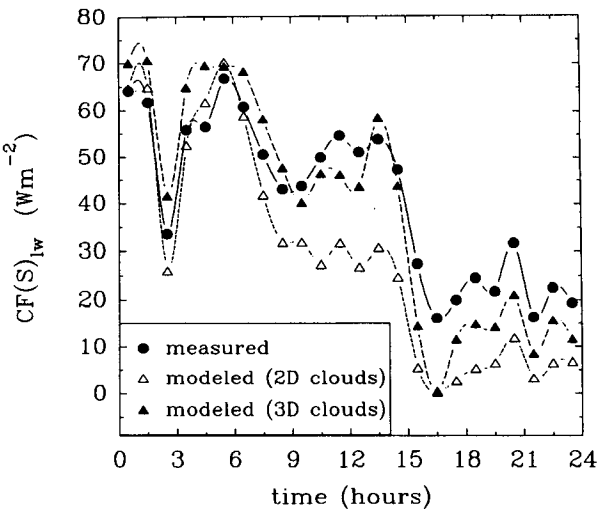

FIG. 4. Comparison of observed and modeled hourly $CF(S)_{lw}$ for 14 June 1992 during ASTEX.

on 14 June could be roughly simulated by the model. A comparison of the modeled and measured $CF(S)_{lw}$ shows that the model simulation does reproduce the observed variation of the $CF(S)_{lw}$. The data labeled modeled (2D clouds) in Fig. 4 correspond to the values of $CF(S)_{lw,2D}$ given by Eq. (3). These results imply that only a very crude treatment of cloud geometry might be necessary to simulate the mean longwave fluxes from layers of finite clouds.

c. *Absolute and effective cloud fractions observed from the ASTEX surface data*

Another meaningful way of quantifying finite-cloud effects in longwave radiation is to compare the values of the absolute cloud fraction N_a and the effective cloud fraction N_e. In this study, N_e is defined as the cloud fraction that accounts for the effect of the clouds' vertical dimensions and spatial arrangements on the longwave fluxes. Using this definition, values of N_e could be expressed as

$$N_e = \frac{F_{sfc} - F_{sfc,clr}}{F_{sfc,ovc} - F_{sfc,clr}} = \frac{CF(S)_{lw}}{CF(S)_{lw,max}}, \qquad (5)$$

where $CF(S)_{lw,max}$ represents the maximum possible value of the $CF(S)_{lw}$, which would occur under overcast conditions. Though surface fluxes were used in computing N_e from the ASTEX data, modeling results showed that values of N_e are relatively independent of height above the surface.

The daily variation of N_e and N_a as observed during ASTEX is shown in Fig. 5. For reference, lines showing the variation for clouds of constant aspect ratio, a_{cld}, are also shown. Here, a_{cld} is defined as the ratio of the cloud's vertical to horizontal dimensions. The lines for

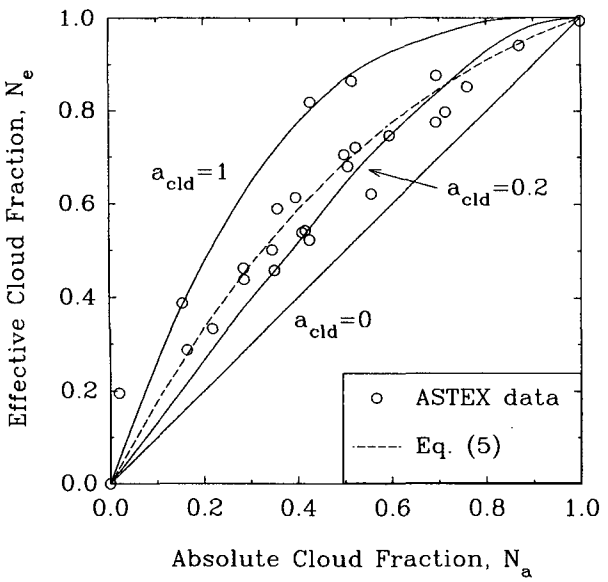

FIG. 5. Observed daily variation of N_e and N_a derived from surface measurements during ASTEX.

clouds of constant a_{cld} were generated using the model described in the next section. As Fig. 5 shows, the daily averaged ASTEX values seem to follow the $a_{cld} = 0.2$ line, with a tendency for the aspect ratio to increase as N_a decreases. An exponential fit of the ASTEX data can be expressed as

$$N_e = N_a \exp[0.6416(1 - N_a)], \quad (6)$$

with the mean rms difference of this fit being 0.11. Though it appears from Fig. 5 that a parameterization of N_e based solely on N_a is possible for the marine stratocumulus regime, the variation of this parameterization for other cloud regimes needs further study.

3. Modeling

In order to examine the effect of finite cloudiness on longwave radiative transfer for a wide range of cloudiness conditions, a three-dimensional radiative transfer model was written. A detailed formulation of this model is given in Heidinger and Cox (1994). The model domain consists of a single horizontally infinite layer of regularly spaced cuboidal clouds embedded in an absorbing and emitting atmosphere. The underlying surface is assumed to behave as a blackbody. Fluxes are calculated along each principal Cartesian axis through a finite integration over azimuth, ϕ, and zenith, θ, angles.

The model spectral region was limited to 11 μm. This region was chosen since it is representative of the 8–12-μm atmospheric window region where most of the longwave cooling in clouds occurs (Stephens 1978). The gaseous absorption characteristics of water vapor at 11 μm were modeled using the method outlined in Roberts et al. (1976). When calculating the absorption and emission of liquid water at 11 μm, a mass absorption coefficient of 0.097 g m^{-2} was used. This value of the mass absorption coefficient was derived from a linear approximation to Mie theory described by Chylek (1978) and is valid for clouds whose 11-μm radiative characteristics are dominated by droplets with radii less than 6 μm.

A major simplifying assumption made in the development of this model was the neglect of the process of scattering in longwave radiative transfer. With this assumption, the cloud forcing radiance I_{cf} at the observer position (x_o, y_o, z_o) along the direction defined by (θ, ϕ) can be expressed in terms of radiative quantities that can be computed separately from one another. To lessen the computational requirements of the model, the model was formulated in terms of the cloud-forcing radiance I_{cf}, which is defined as the difference between the actual radiance and the clear sky radiance. Once the model computed the cloud-forcing radiance field, the predetermined clear sky radiances were added to the cloud-forcing radiances to give the actual radiance field. In the following quantities, the superscripts "+" and "−" refer to upwelling ($\theta > 90°$) and downwelling directions ($\theta < 90°$), respectively. For a downwelling line of sight ($\theta < 90$), I_{cf}^- can be expressed as

$$I_{cf}^-(x_o, y_o, z_o, \theta, \phi) = T_{sc}[(T_{cld} - T_{cldgas})I_{ac}^- + (I_{cld}^- - I_{cldgas}^-)], \quad (7)$$

where T_{sc} is the 11-μm transmission from the observer to the cloud layer. The transmission through and emission from the cloud layer due to the atmospheric water vapor is represented by T_{cldgas} and I_{cldgas}^-, and T_{cld} and I_{cld}^- are the transmission and emission from the cloud layer due to the presence of both cloud water and water vapor: I_{ac}^- is the downwelling radiance above the cloud layer. Similarly, an expression for the cloud forcing radiance for the upwelling directions is

$$I_{cf}^+(x_o, y_o, z_o, \theta, \phi) = T_{ac}[(T_{cld} - T_{cldgas})I_{sc}^+ + (I_{cld}^+ - I_{cldgas}^+)] + T_{ac}T_{sc}(T_{cld} - T_{cldgas})I_{sfc}^+, \quad (8)$$

where T_{ac} is the 11-μm transmission from the observer to the cloud layer, and I_{sc}^+ and I_{sfc}^+ represent the upwelling radiance due to emission from the subcloud layer and the surface, respectively.

Note that if a line of sight does not intercept a cloud, the cloud forcing radiance is zero, and the value of I_{cf}^+ is always zero below the cloud layer, as is the value of I_{cf}^- above the cloud layer. The emission from each model layer was accomplished by assuming that the emission was linear in optical depth, as outlined in Ackerman et al. (1990). For simulations where the atmosphere is assumed to be transparent to 11-μm radi-

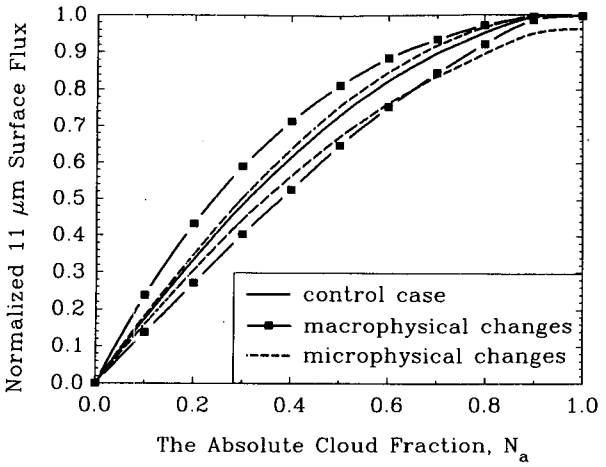

FIG. 6. The sensitivity of the 11-μm surface flux to macrophysical and microphysical changes in simulated cumulus clouds. The control case corresponds to clouds with an optical depth of 4 and an aspect ratio of 0.5. Macrophysical and microphysical changes correspond to doubling and halving the cloud aspect ratio and optical depth, respectively.

ation, the values of T_{sc}, T_{ac}, and T_{cldgas} are set to unity, and values of $I^{+/-}_{cldgas}$ and I^{-}_{ac} are set to zero. The methods for computing the radiances and transmissions used in Eqs. (7) and (8) are given in Heidinger and Cox (1994).

Model results

Before applying the model described above to the task in the next section, a few modeling results of general interest are now presented. Though much research recently has focused on the effects of the cloud microphysical properties on longwave radiative transfer, the following exercise will illustrate how cloud macrophysical properties can dominate the transfer of longwave radiation in the presence of partial cloudiness. Imagine a control case consisting of a cuboidal cloud with an aspect ratio, a_{cld}, of 0.5 and an optical depth, τ, of 4. In this simulation, microphysical changes were accomplished by changes in τ, and macrophysical changes were accomplished by changes in a_{cld}. To explore the sensitivity of the 11-μm downwelling flux to microphysical changes, the optical depth of the control cloud was halved and doubled, while the macrophysical properties were unchanged. Similarly, the sensitivity of the downwelling flux to macrophysical changes was explored by halving and doubling a_{cld} while keeping τ constant. The results of the variation of the 11-μm flux for the microphysical and macrophysical changes described above are shown in Fig. 6 for values of N_a ranging from clear to overcast conditions. As Fig. 6 shows, when clouds are optically thick, an accurate macrophysical definition of a cloud layer may be more crucial than a detailed microphysical definition in the calculation of fluxes in the presence of broken cloudiness. Though clouds with $\tau = 4$ are nearly blackbodies, this exercise is relevant since most boundary layer clouds are sufficiently optically thick to be considered blackbodies.

A comparison of the variation of N_e and N_a for optically thick cuboidal clouds computed by the model described above and with results published by Harshvardhan and Weinman (1982) is shown in Fig. 7. In this simulation, the clouds were assumed to be isothermal and to be embedded in a transparent atmosphere. As Fig. 7 shows, N_e is always greater than N_a except for conditions of clear and overcast skies. A comparison of these two results for any value of a_{cld} and N_a shows that the values of N_e reported by Harshvardhan and Weinman are significantly less than those produced by this study. The measurements of N_e published by Harshvardhan and Weinman (1982) were based on a light table experiment where reflected light may have caused the underestimation of N_e shown in Fig. 7. Also shown in Fig. 7 is an estimate of N_e for $N_a = 0.5$ and $a_{cld} = 1.0$ for regularly spaced cuboidal clouds arranged in a checkerboard pattern by standard radiation view factor calculations (Incropera and Dewitt 1990). Since the results from this model seem to agree with the theoretical calculations, the parameterization of N_e based on N_a and a_{cld} presented in Harshvardhan and Weinman (1982) was modified to fit the results produced in this study as

$$N_e = \frac{[1 + 1.27a_{cld}(1 + 5.75N_a)]N_a}{1 + 1.27a_{cld}N_a(1 + 5.75N_a)}. \quad (9)$$

For comparison, results for a random distribution (Ellingson 1982) and a fractal distribution (Killen and

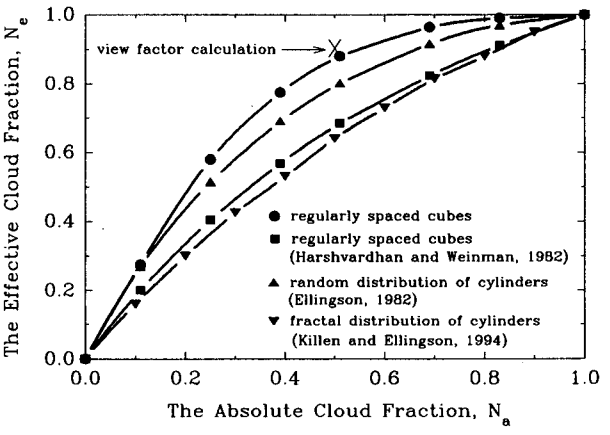

FIG. 7. Variation of N_e with N_a for different cloud geometries and spatial arrangements. All simulated clouds are isothermal, optically thick, and embedded in a transparent atmosphere. The ratio of the height to width for all clouds is unity.

Ellingson 1994) of right circular cylindrical clouds are shown in Fig. 7. The simulated clouds are again isothermal and optically thick, and the ratio of the cloud height to cloud diameter was unity. Since a regularly spaced distribution of clouds allows the clouds' sides to have a maximum effect on the fluxes exiting a finite-cloud layer, one would expect values of N_e from random or fractal distributions to be smaller than the value from a regularly spaced array. A detailed discussion of the effects of the spatial distribution and cloud shape on value of N_e for layers of finite clouds is given in Killen and Ellingson (1994).

4. Inclusion of finite-cloud effects in one-dimensional longwave radiative transfer schemes

The previously presented ASTEX observations and three-dimensional modeling studies have shown that finite-cloud effects can significantly alter longwave radiative transfer. As demonstrated by the magnitude of the finite-cloud effects in the $CF(S)_{lw}$ from ASTEX, this sensitivity of longwave radiative transfer to finite-cloud effects is large enough to warrant the inclusion of these effects into numerical weather and climate prediction models. Due to the computational requirements of 3D radiative transfer schemes, the inclusion of finite-cloud effects into numerical weather and climate prediction models requires that these effects be incorporated into the existing computationally efficient 1D plane-parallel radiative transfer schemes. This section will compare three different techniques that allow 1D radiative transfer schemes to account for 3D finite-cloud effects.

Up to this point, the discussion of finite-cloud effects in longwave radiative transfer has been limited to the longwave surface flux. However, the quantity most useful to numerical weather and climate models is the radiative heating rate. Therefore, the different 1D finite-cloud methods will be judged on their ability to reproduce the horizontally averaged heating rates calculated by the 3D radiative transfer model discussed in section 3. The longwave heating rate $H(z)$ can be expressed in terms of the vertical divergence of the net vertical flux as

$$H(z) = -\frac{1}{\rho c_p}\frac{\partial F_{\text{net}}}{\partial z}, \qquad (10)$$

where $F_{\text{net}} = F_z^+ - F_z^-$. Note that the horizontal flux divergence was ignored in the calculation of these heating rates. Since the quantities presented in this chapter are horizontally averaged through a cloud layer that is horizontally infinite, the horizontal flux divergence is zero. This would not be the case if the horizontal averaging were done only over an individual cloud where the horizontal flux divergences do create enhanced cooling along the lateral sides of the cloud.

Three methods were chosen as candidates for the inclusion of 3D finite-cloud effects into 1D longwave radiative transfer codes. Only methods that could be relatively easily implemented into existing 1D radiative transfer schemes were examined. The three 1D finite-cloud methods are listed below:

1) a weighting scheme based on N_a,
2) a weighting scheme based on N_e, and
3) a scheme based on a linear variation of $N_e^{+/-}$ through the cloud layer.

Traditionally, radiative transfer in the presence of partial cloudiness has been solved by weighting the plane-parallel solutions for clear and overcast sky conditions. The most commonly used weight in this method is the absolute cloud fraction N_a. The use of N_a as the weighting factor allows $H(z)$ to be computed as

$$H(z) = N_a H_{\text{ovc}}(z) + (1 - N_a)H_{\text{clr}}(z), \qquad (11)$$

where $H_{\text{clr}}(z)$ and $H_{\text{ovc}}(z)$ are the plane-parallel heating rates for clear and overcast sky conditions, respectively.

As discussed earlier, the use of N_a in the above weighting scheme ignores the radiative effect of the vertical dimensions of clouds. One obvious way to incorporate the effects of the 3D geometry of the cloud layer would be to replace N_a in the above weighting scheme with N_e, the effective cloud fraction (Stephens 1984). For example, when parameterizing fractional cloudiness in a two-stream model, Schmetz (1984) used the N_e parameterization given by Harshvardhan and Weinman (1982). Using such a scheme, the horizontally averaged heating rate profile is computed as

$$H(z) = N_e H_{\text{ovc}}(z) + (1 - N_e)H_{\text{clr}}(z). \qquad (12)$$

Though this method produces accurate results compared to the 3D model outside of the cloud layer, the results of the next section will show that the magnitude of the heating profile through the cloud layer predicted by this method can be in significant error.

The two 1D finite-cloud methods discussed above are simple weighting schemes based on a constant cloud fraction. Though the values of N_e and N_a are relatively independent of height outside of the cloud layer, N_e does have a directional dependence in the cloud layer. The height dependence of N_e outside the cloud layer varies depending on the amount of atmospheric absorption between the observer and the cloud layer and, thus, on the spectral region of interest. These effects are relatively minor, and values of N_e can be considered constant with height outside the cloud layer and without any spectral variation. A more in-depth discussion of these effects is given in Heidinger and Cox (1994).

As mentioned, values of N_e take on a directional dependence inside of the cloud layer. To incorporate this directional dependence, let N_e^+ and N_e^- be used to

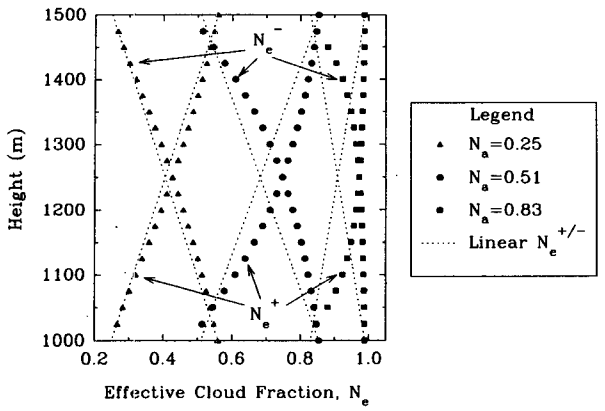

FIG. 8. Variation of $N_e^{+/-}$ through simulated layers of cubic clouds for $N_a = 0.25$, 0.51, and 0.83.

weight the upwelling and downwelling fluxes, respectively. Using N_e^+ and N_e^-, the upwelling and flux at level z, $F^+(z)$, can be written as

$$F^+(z) = N_e^+(z)F^+_{\text{ovc}}(z) + (1 + N_e^+(z))F^+_{\text{clr}}(z), \quad (13)$$

and the downwelling flux at level z, $F^-(z)$, can be written as

$$F^-(z) = N_e^-(z)F^-_{\text{ovc}}(z) + (1 - N_e^-(z))F^-_{\text{clr}}(z), \quad (14)$$

where F_{clr} and F_{ovc} are the clear and overcast sky fluxes computed by plane-parallel theory. One point to note is that above the cloud layer, N_e^- becomes meaningless, as does N_e^+ below the cloud layer. Physically, one can imagine that $N_e^{+/-}$ will vary from N_e to N_a through the cloud layer, where N_e is the quasi-constant value of the effective cloud fraction relative to an observer positioned outside the cloud layer. For example, at the base of the cloud layer, N_e^- will have the value of N_e. As the observer approaches the cloud top from below, the relative aspect ratio of the clouds becomes smaller and smaller. As the observer closes in on the cloud top, the relative cloud aspect ratio becomes very small, and, as predicted by Eq. (9), N_e^- approaches the value of N_a. Similarly, N_e^+ can be imagined to vary between N_e near the cloud top and N_a near the cloud base. One way to account for these variations is to assume that both $N_e^{+/-}$ vary linearly through the cloud layer. The heating rates calculated by this 1D finite-cloud method were calculated by a finite differencing of the net flux profiles generated by Eqs. (13) and (14).

The 1D finite-cloud method described above was based on the assumption that $N_e^{+/-}$ varied linearly through the cloud layer. To test the validity of this assumption, a 3D simulation was performed of a cloud field consisting of an evenly spaced array of isothermal 500-m cubic clouds ($a_{\text{cld}} = 1$), with each having a vertically homogeneous liquid water content of 0.2 g m^{-3}. The dimensions of these clouds are similar to the boundary layer cumuli observed by Stull (1984), and the liquid water content is representative of values typically observed in stratus and stratocumulus clouds (Stephens 1978). Since the cooling in the cloud layer is dominated by the cloud water, the presence of atmospheric water vapor was ignored in these simulations. Figure 8 shows the actual variation of $N_e^{+/-}$ through the cloud layer for three different values of N_a. Differing values of N_a were simulated by varying the spacing between the clouds. As given by the parameterization in Eq. (9), the $N_a = 0.25$, 0.51, and 0.83 simulations yielded values of $N_e = 0.58$, 0.86, and 0.98, respectively. As Fig. 8 shows, the values of $N_e^{+/-}$ for each simulation vary between N_a and N_e through the cloud layer. Also plotted in Fig. 8 are the assumed linear profiles. A comparison of the linear and actual $N_e^{+/-}$ profiles shows the validity of the linear approximation decreases with increasing values of N_a. The effect of this increasing nonlinearity with increasing N_a will be shown below.

Comparison of the 1D longwave finite cloud parameterization methods

To test the accuracy of the 11-μm heating rate profiles predicted by each of the 1D finite-cloud methods, a 3D model simulation was performed. The simulated cloud field again consisted of cubic clouds with horizontal widths of 500 m arranged to give a value of 0.25 for N_a. The liquid water content of the clouds was 0.2 g m^{-3} and was vertically uniform. A temperature of 280 K was assumed for the clouds, and the underlying surface was assumed to radiate as a blackbody at 290

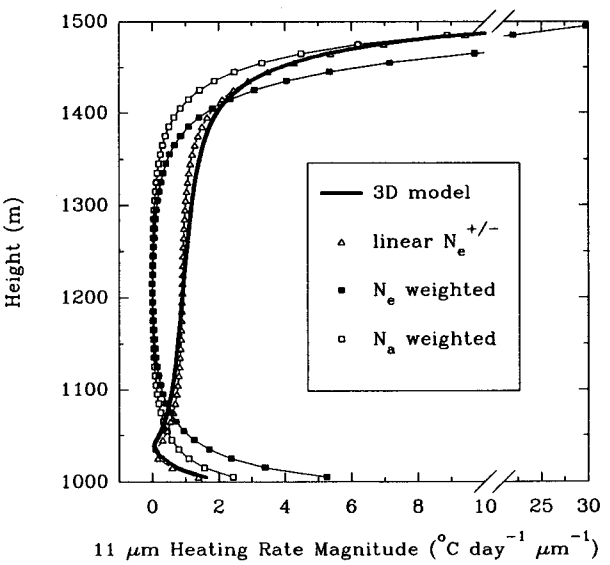

FIG. 9. Comparison of the horizontally averaged 11-μm heating rate profiles for the $N_a = 0.25$ simulation.

K. As before, the effects of atmospheric water vapor were ignored in this simulation. Since atmospheric water vapor was neglected, no radiative heating occurred outside of the cloud layer. All the results presented here are for the 11-μm spectral region.

Figure 9 shows a comparison of the 11-μm heating rate profiles through the cloud layer predicted by the 3D model and each of the 1D finite-cloud methods described above. To aid in the comparison, the heating rate profiles in Fig. 9 are plotted as heating rate magnitudes. The actual radiative heating rate profiles show warming near the cloud base and strong cooling near the cloud top. Since the 3D model accounted for the effects of the 3D variation in the cloud geometry and radiance fields, its results were used as the basis for a comparison of the different 1D methods for the inclusion of finite-cloud effects into 1D radiative transfer schemes.

Inspection of the results in Fig. 9 shows that the N_a weighting scheme accurately predicted the heating rates both near the cloud-base top and the cloud base. The N_e weighting scheme, however, significantly overestimated the cloud-top cooling and the cloud-base warming. Since the overcast and clear sky heating rate values in the center of the cloud region are near zero, both the N_a and N_e weighting schemes predicted near-zero cooling in the cloud layer away from the cloud base and top (1100–1400 m). Due to significant cooling near the lateral edges of the clouds, however, the 3D model results showed approximately a 1°C day^{-1} cooling near the center of the cloud layer. Clearly, any simple weighting scheme based on plane-parallel calculations would be unable to reproduce the 3D heating rate profile through the cloud layer.

Also shown in Fig. 9 is the heating rate profile predicted by the 1D finite-cloud method, which assumed the linear profile of $N_e^{+/-}$ shown in Fig. 8. A comparison of the results shows that not only did the linear $N_e^{+/-}$ method accurately reproduce the 11-μm heating rates near the cloud base and top, but this method also approximately reproduced the cooling in the central regions of the layer.

As Fig. 9 shows, the linear $N_e^{+/-}$ parameterization method produced a heating profile that was significantly more accurate compared to the 3D model results than either the N_e or N_a weighting schemes for the simulation with $N_a = 0.25$. As mentioned previously, the variation of $N_e^{+/-}$ through the cloud layer becomes less linear as the cloud fraction increases. A comparison of the errors associated with each 1D finite-cloud parameterization method as a function of N_a is shown in Fig. 10. These simulations are identical to the $N_a = 0.25$ simulation described above except that the spacing between the clouds was varied to generate the differing values of N_a. The results in Fig. 10 are presented as the mean 11-μm heating rate error, which can be expressed as

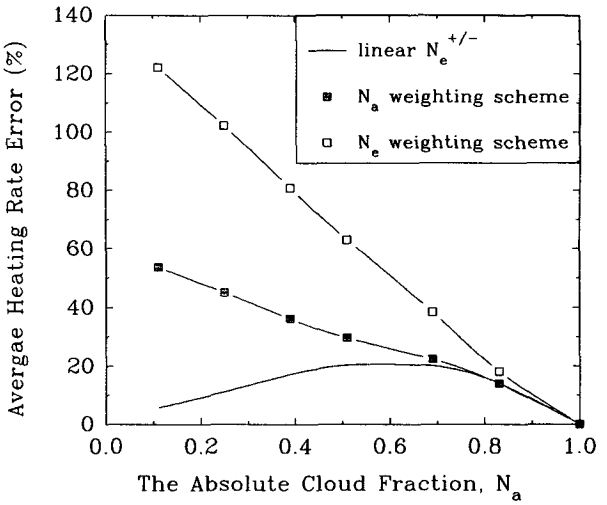

FIG. 10. Comparison of the average 11-μm heating rate errors for the simulated cubic clouds from the three 1D finite-cloud parameterization methods.

$$H_{\text{err}} = \frac{\int_{z_b}^{z_t} |\bar{H}_{3D}(z) - H_{1D}(z)|\, dz}{\int_{z_b}^{z_t} |\bar{H}_{3D}(z)|\, dz}, \qquad (15)$$

where $H_{3D}(z)$ is the horizontally averaged heating rate from the 3D model and $H_{1D}(z)$ is the heating rate predicted by any of the 1D finite-cloud methods. As Fig. 10 shows, the errors associated with the linear $N_e^{+/-}$ method are considerably less than those associated with the N_a and N_e weighting schemes for values of N_a less than 0.7. Only for high values of cloud fraction do the errors from the linear $N_e^{+/-}$ method and the other methods become comparable.

Another consideration of any 1D finite-cloud parameterization method is the ability to accurately reproduce the net heating of the cloud layer. Since the linear $N_e^{+/-}$ and the N_e weighting scheme accurately reproduced the fluxes exiting from the cloud layer, the total heating of the cloud predicted by these methods and the 3D model was identical. The N_a weighting scheme, however, underestimated the net cooling of the cloud significantly due to its underestimation of the flux exiting the cloud layer at the cloud base and its overestimation of the flux exiting the cloud layer from the cloud top. As described by Harshvardhan and Weinman (1982), the relative magnitude of this underestimation of the net cooling by the N_a weighting scheme is equal to the ratio of N_a to N_e in the case of optically thick isothermal clouds.

In summary, of the 1D finite-cloud parameterization methods discussed, only the method that assumed a linear variation of $N_e^{+/-}$ through the cloud layer repro-

duced the net cooling in the cloud layer and effectively simulated the heating rate profile through the cloud layer when compared to the 3D model results. In addition, model simulations were performed to test the sensitivity of the results of this 1D finite-cloud parameterization method to irregular cloud geometries and vertically inhomogeneous cloud liquid water contents. The simulations showed that the variation of $N_e^{+/-}$ was independent of the cloud geometry of the cloud layer. This result indicated that any two cloud layers with the same average values of N_a and a_{cld} will have the same relative profile of $N_e^{+/-}$ through the cloud layer. To more realistically approximate the stratocumuli liquid water profiles observed by Duda et al. (1991), the liquid water content of the clouds was assumed to increase linearly from cloud base to cloud top with a mean value of 0.2 g m^{-3}; these simulations showed that the linear $N_e^{+/-}$ methods suffered no loss of accuracy for these conditions.

5. Conclusions

This research focused on the role of finite-cloud effects in longwave radiative transfer. Clouds have been known for decades to be a fundamental modulator of radiation in the earth's atmosphere. As numerical weather and climate models begin to deal with the subgrid-scale distributions of cloudiness, the inclusion of the effect of the finite dimensions of clouds on radiative transfer becomes imperative.

One of the strengths of this research was the ability to show directly finite-cloud effects in measurements of the longwave surface flux. The observations used in this study were collected during the ASTEX phase of FIRE during June 1992 on the island of Porto Santo. The analysis of these measurements showed that longwave surface flux schemes that ignored the vertical dimensions of the clouds typically underestimated the longwave surface forcing by 9 W m^{-2} on average out of a total longwave cloud forcing of 30 W m^{-2}. These values from the ASTEX region should be representative of any fair weather cumulus cloud field.

This research investigated the parameterization and inclusion of these finite-cloud effects into existing one-dimensional radiative transfer schemes. Several different methods for the inclusion of finite-cloud effects were compared. The commonly used method of accounting for partial cloudiness by weighting overcast and clear sky flux profiles by the absolute cloud fraction N_a was found to significantly underestimate the net cooling in cloud layers. A method that accurately predicted both the net cooling and the distribution of cooling in the cloud assumed a linear variation of the effective cloud fraction N_e through the cloud layer. Due to the simplicity of this method, current one-dimensional longwave radiative transfer schemes could easily be modified to account for finite-cloud effects. In addition, a parameterization of N_e based on the absolute cloud fraction N_a developed from the ASTEX data was presented.

Through the observations and modeling simulations presented here, the role of finite-cloud effects in longwave radiative transfer was shown to be worthy of further study. In this research, the effective cloud fraction was shown to be a useful quantity in characterizing finite-cloud effects. Since routine measurements of N_e are not currently made, one beneficial area of future research might be the measurement of this important quantity on a global basis. Once the variation of N_e is known globally, comprehensive studies of finite-cloud effects in longwave radiative transfer would then be possible.

Acknowledgments. We would like express our appreciation for the technical assistance of J. Davis, our colleague at Colorado State University. We further thank R. Kropfli and J. Snider of NOAA/ERL for making the 8.7-mm radar data and the microwave-radiometer-derived liquid water path data available to us. This research was supported by NASA Contract NAG-1-1146 and ONR Contract N00014-91-J-1422.

REFERENCES

Ackerman, S. A., W. L. Smith, J. D. Spinhirne, and H. E. Revercomb, 1990: The 27–28 October 1986 FIRE IFO cirrus case study: Spectral properties of cirrus clouds in the 8–12-μm window. *Mon. Wea. Rev.*, **118,** 2377–2388.

Albrecht, B. A., and S. K. Cox, 1976: Pyrgeometer data reduction and calibration procedures. Colorado State University Atmospheric Science Paper 251, Dept. of Atmos. Sci., Colorado State University, 48 pp.

Chylek, P., 1978: Extinction and liquid water content of fogs and clouds. *J. Atmos. Sci.*, **35,** 296–300.

Cox, S., S. Gillies, A. Heidinger, and C. Keith, 1993: CSU ASTEX surface data sets from Porto Santo (June 1–28, 1992). Colorado State University Atmospheric Science Paper 530, Dept. Of Atmos. Sci., Colorado State University, 146 pp.

Duda, D. P., G. L. Stephens, and S. K. Cox, 1991: Microphysical and radiative properties of marine stratocumulus from tethered balloon measurements. *J. Appl. Meteor.*, **30,** 170–186.

Ellingson, R. G., 1982: On the effects of cumulus dimensions on longwave irradiance and heating rate calculations. *J. Atmos. Sci.*, **39,** 886–896.

Evans, K. F., 1993: A general solution for stochastic radiative transfer. *Geophys. Res. Letters,* **20,** 2075–2078.

Gupta, S. K., W. F. Staylor, W. L. Darnell, A. C. Wilber, and N. A. Ritchey, 1993: Seasonal variation of surface and atmospheric cloud radiative forcing over the globe derived from satellite data. *J. Geophys. Res.*, **98,** 20 761–20 778.

Harshvardhan, and J. A. Weinman, 1982: Infrared radiative transfer through a regular array of cuboidal clouds. *J. Atmos. Sci.*, **39,** 431–439.

——, J. A. Weinman, and R. Davies, 1981: Transport of infrared radiation in cuboidal clouds. *J. Atmos. Sci.*, **38,** 2500–2513.

Heidinger, A., and S. Cox, 1994: Finite cloud effects in longwave radiative transfer. Colorado State University Atmospheric Science Paper 563, Dept. Of Atmos. Sci., Colorado State University, 104 pp.

Incropera, F. P., and D. P. Dewitt, 1990: *Fundamentals of Heat and Mass Transfer.* 3d ed., J. Wiley and Sons, 919 pp.

Killen, R. M., and R. G. Ellingson, 1994: The effect of shape and spatial distribution of cumulus clouds on longwave irradiance. *J. Atmos. Sci.,* **51,** 2123–2136.

Liou, K. N., and S. C. Ou, 1979: Infrared radiative transfer in finite cloud layers. *J. Atmos. Sci.,* **36,** 1985–1996.

Niylisk, Kh., 1968: Atmospheric thermal radiation in partly cloudy regions. *Atmos. Oceanic Phys.,* **4,** 383–396.

——, 1972: Cloud characteristics in problems of radiation energetics in the earth's atmosphere. *Atmos. Oceanic Phys.,* **8,** 270–281.

Plank, V. G., 1969: The size distribution of cumulus clouds in representative Florida populations. *J. Appl. Meteor.,* **8,** 46–67.

Roberts, R. E., L. M. Biberman, and J. E. A. Selby, 1976: Infrared continuum absorption by atmospheric water vapor in the 8–12 μm window. *Appl. Opt.,* **15,** 2085–2090.

Schmetz, J., 1984: On the parameterization of the radiative properties of broken clouds. *Tellus,* **36A,** 417–432.

Stephens, G. L., 1978: Radiation profiles in extended water clouds. I: Theory. *J. Atmos. Sci.,* **35,** 2111–2122.

——, 1984: The parameterization of radiation of numerical weather prediction and climate models. *Mon. Wea. Rev.,* **112,** 826–867.

——, and R. W. Preisendorfer, 1984: Multimode radiative transfer in finite optical media. II: Solutions. *J. Atmos. Sci.,* **41,** 725–735.

Stull, R. B., 1984: Models and measurements of the interaction between the mixed layer and fair-weather cumulus clouds; Part 2. Some preliminary measurements. *Transactions of An APCA Specialty Conference on Environmental Impact of Natural Emissions,* V. P. Aneja, Ed., Air Pollution Control Association, 326–337.